
Jamais Vu: Exposing the Generalization Gap in Supervised Semantic Correspondence

Octave Mariotti¹ Zhipeng Du¹ Yash Bhalgat² Oisin Mac Aodha¹ Hakan Bilen¹

¹University of Edinburgh

²University of Oxford

Abstract

Semantic correspondence (SC) aims to establish semantically meaningful matches across different instances of an object category. We illustrate how recent supervised SC methods remain limited in their ability to generalize beyond sparsely annotated training keypoints, effectively acting as keypoint detectors. To address this, we propose a novel approach for learning dense correspondences by lifting 2D keypoints into a canonical 3D space using monocular depth estimation. Our method constructs a continuous canonical manifold that captures object geometry without requiring explicit 3D supervision or camera annotations. Additionally, we introduce SPair-U, an extension of SPair-71k with novel keypoint annotations, to better assess generalization. Experiments not only demonstrate that our model significantly outperforms supervised baselines on unseen keypoints, highlighting its effectiveness in learning robust correspondences, but that unsupervised baselines outperform supervised counterparts when generalized across different datasets.

1 Introduction

The task of semantic correspondence (SC) estimation involves identifying semantically matching regions across different instances of the same object category. It remains a challenging problem, as it requires recovering fine-grained details while maintaining robustness against variations in appearance and shape. Recent advances in large-scale vision models, particularly self-supervised transformers [6, 35] and generative diffusion models [37], have led to notable improvements in SC. When employed as backbones, these models have achieved over 20% gains in accuracy on the SPair-71k benchmark [30]. However, despite these advances, recent studies have highlighted that these powerful representations often struggle to disambiguate symmetric object parts due to their visual similarity [54, 29].

SC methods can be broadly categorized into two groups in terms of supervision: unsupervised models, which do not require correspondence annotations during training [1, 2, 53, 29], and supervised models [8, 17, 54], which are trained on annotated correspondences. As expected, supervised models generally achieve higher performances when using the same backbone and same training set as unsupervised models. However, a key limitation of current benchmarks is that evaluation is typically performed on the *same* set of keypoints used for training, potentially inflating perceived generalization. As illustrated in Fig. 1, the performance of supervised models drops significantly when evaluated on unseen keypoints, while unsupervised models maintain their performance.

Building dense correspondences are key to fine-grained object understanding and improving robustness in various recognition tasks, and essential to many applications including texture transfer [34] and robotic manipulation [43]. In this paper, we examine the performance of state-of-the-art SC models when evaluated on points that lie outside the set of annotated training keypoints. Under these conditions, we observe that supervised pipelines often underperform their unsupervised counterparts, effectively reducing their function to that of ‘sparse keypoint detectors’. We attribute this limitation

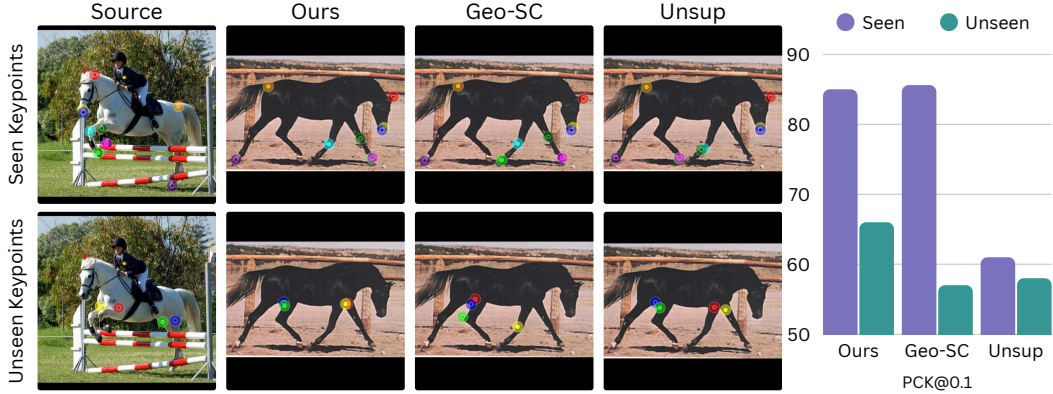


Figure 1: **Illustration of the generalization gap on unseen keypoints.** (Left) Top row: when evaluated on known keypoints, both our model and Geo-SC [54] perform well while the unsupervised DINOv2+SD [53] struggles to correctly disambiguate the legs of the horse. Bottom row: when presented with keypoints unseen at training time, both our model and DINO+SD predict noisy but reasonable correspondence, while Geo-SC predictions noticeably degrade. (Right) Even though it obtains strong performance on known keypoints, Geo-SC performs worse than its unsupervised counterpart on our new benchmark of unseen keypoints. In comparison, our model still achieves competitive results.

to two main factors: (i) the sparsity of supervision, which typically focuses on a limited number of keypoints and (ii) the lack of evaluation on unseen points, which tends to favor models that bias their predictions toward the nearest seen annotations.

We argue that an ideal SC method should be capable of matching arbitrary points, akin to the objectives in classical dense correspondence tasks [23]. To move beyond sparse supervision, we propose a learning framework that predicts dense feature maps and supervises them using geometry from an off-the-shelf depth estimator, thereby enabling training on richer and more spatially diverse cues. Few unsupervised SC methods [42, 29] have leveraged 3D geometry to learn dense correspondences through mapping object pixels to a spherical coordinate system where each coordinate corresponds to a different characteristic point of the object. However, this approach requires estimating the object shape and viewpoint from a collection of 2D images, which limits to the applicability of such models to synthetically generated datasets [42] or relying on camera viewpoint supervision [29].

We propose a new approach that leverages existing 2D keypoint annotations and estimated 3D geometry to learn dense correspondences without requiring any direct 3D supervision. We build on the idea of learning a canonical representation of the object category, which is invariant to the object instance, viewpoint, and pose. We achieve this by lifting the 2D keypoints to 3D using a monocular depth model, aligning them with a set of canonical keypoints that are shared across all instances of the object category. Finally, by interpolating between them, we learn a continuous canonical manifold, that captures the underlying 3D shape of the object and incorporates geometric constraints into learning more effective and general feature representations. We also introduce a new dataset for SC, SPair-U which extends the original SPair-71k test annotations with a set of new keypoints, allowing us to evaluate the generalization of SC models to unseen keypoints. We show that supervised SC models trained on the original SPair-71k dataset typically fail to generalize well to unseen keypoints, while our method is able to learn a more general representation that can be applied to unseen keypoints.

2 Related Work

Supervised methods. Supervised approaches rely on the availability of datasets with annotated keypoints such as CUB [44], PF-PASCAL [14], and SPair-71k [30] to learn corresponding points across instances of the same object class depicted in different images. This is typically using contrastive objectives minimizing distance between features coming from the same keypoints while pushing other features away [15, 40, 53, 54]. Flow-based approaches, that compute 4D correlations maps between source and target images have also been explored [8, 17]. To obtain stronger descriptors, it is also common to aggregate features from multiple network layers to form hypercolumns [31, 1, 54]. Current state-of-the-art supervised methods forego training from scratch and instead typically use a

large pretrained vision model as a backbone, the most popular options being DINOv2 [35] and Stable Diffusion [37]. While effective at matching instances of keypoints of the same type that have been observed during training, in our experiments we demonstrate that current supervised methods have a tendency to overfit to the set of keypoints observed during training and struggle to generalize to previously unseen keypoints (see Fig. 1 for an example).

There have also been recent attempts to utilize the expressive power of the representations encoded in large multi-modal models for detecting sets of keypoints. Few-shot methods require supervision in the form of a support set at inference time [25, 26, 16]. Zero-shot methods forego the need for such supervision, but instead require that keypoints should be described via natural language prompts [55, 52]. Describing common keypoints (e.g., ‘the left eye’) can be easily done via language, but how to best describe less salient points via text is not so clear. There have also been attempts to develop models that can take different various modalities (i.e., text and or keypoints) as input [27]. While promising, these methods make use of large multi-modal models and need large quantities of keypoint supervision data, spanning many diverse keypoints and categories, for pretraining.

Unsupervised / weakly-supervised methods. Methods that do not use correspondence supervision during training range from completely unsupervised approaches [42, 41, 2, 1, 53], zero-shot methods that only use test-time information about the relationships between keypoints [34, 54], dense methods that directly impose structure on the correspondence field [7], and weakly supervised methods that use extra labels like segmentation masks or camera pose [19, 29, 4]. Earlier unsupervised methods typically use self-supervised objectives that make use of synthetic deformations/augmentations of the same image [42] or by using cycle consistencies [41] to provide pseudo ground truth correspondence. Later it was observed that large pretrained vision models naturally possess features that are very strong for SC, despite not being trained on this task explicitly. As a result, more recent unsupervised methods tend to not train their own backbones from scratch and instead explore ways to aggregate [1, 53], or align [13, 29] these features across images.

Geometry-aware methods. Inspired by the classic correspondence setting in vision that relies on geometric constraints to match the same 3D locations across views [10, 38], utilizing geometry cues is an effective way to learn SC. For SC, the underlying assumption is that different instances from the same object category share a similar spatial structure. Flow and rigidity constraints are often used in tracking [46, 50] and unsupervised SC [13, 4]. Recent studies have shown that ambiguities caused by symmetric objects are a major source of errors in SC [54, 29]. One potential way to mitigate these errors is to develop 3D-aware methods. Initially, this has been explored by building correspondence across images by matching points along the surface of objects to 3D meshes [56, 22, 33], but the requirement for meshes greatly limits the applicability of these approaches.

More recently, methods have been proposed to learn 3D shape from image collections [32, 49, 3]. However, these methods require solving multiple problems at once, i.e., estimating object shape, deformations, camera pose, and are therefore limited to specific types of object categories and tend to break easily when applied to more complex shapes. Recent advances in monocular depth [36, 5, 20, 51, 12, 47] and geometry prediction [48] allows for reliable geometry estimation from a single image, which can be leveraged for imparting 3D-awareness into SC methods.

Concurrent work [45], also proposes to geometrically align images in 3D using depth maps to build category prototypes. However, it is designed around a test-time alignment of the 3D prototype to the test image, which requires segmentation masks, and lacks the ability to generalize to new categories, as no prototype for them would exist in absence of training samples.

3 Method

3.1 Overview

Let $I \in \mathbb{R}^{H \times W \times 3}$ be an RGB image of the object, defined over the image domain $\Lambda \in \mathbb{R}^2$, a lattice of size $H \times W$. Our objective is to learn a function $\Phi(I, \mathbf{u}) \rightarrow \mathbf{z}$, which maps each pixel coordinate $\mathbf{u} \in \Lambda$ to a descriptor $\mathbf{z} \in \mathbb{R}^M$. The descriptor \mathbf{z} should be semantically consistent (e.g., left eye of a cat), meaningfully aligned across different images of objects from the same category, and be invariant to changes in pose and shape. Once Φ is learned, semantic correspondence can be established by finding, for a pixel \mathbf{u} in image I , the most similar pixel \mathbf{u}' in another image I' of the same object

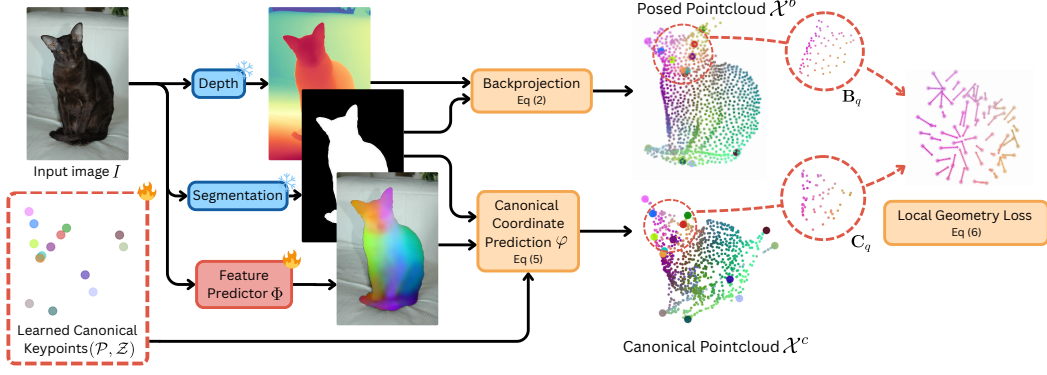


Figure 2: **Overview of our approach.** We extract segmentation masks and depths maps for training images and backproject object points to produce the posed point clouds \mathcal{X}^b . We predict dense features with Φ and match them against our jointly learned sparse category prototype $(\mathcal{P}, \mathcal{Z})$ to produce the canonical point clouds \mathcal{X}^c . The local geometric alignment between the two provides supervision for updating Φ .

category. This is done by querying nearest-neighbor matching in descriptor space according to distance d , typically the cosine distance, i.e., $d(\mathbf{a}, \mathbf{b}) = 1 - \langle \mathbf{a}, \mathbf{b} \rangle / (\|\mathbf{a}\|_2 \|\mathbf{b}\|_2)$:

$$\mathbf{u}' = \arg \min_v d(\Phi(I, \mathbf{u}), \Phi(I', \mathbf{v})). \quad (1)$$

In the standard supervised SC task, we are given a training set, $\{(I^{(1)}, \mathcal{K}^{(1)}), \dots, (I^{(N)}, \mathcal{K}^{(N)})\}$ where each image $I^{(n)}$ is annotated with a sparse set of semantic keypoints $\mathcal{K} = \{\mathbf{k}_1, \dots, \mathbf{k}_{|\mathcal{K}|}\}$ where $\mathbf{k} \in \Lambda$. A common strategy, adopted in recent works [17, 8, 9, 28, 53, 54], is to learn a descriptor function $\Phi(I, \mathbf{u})$ that produces a local descriptor \mathbf{z} for each pixel \mathbf{u} in I such that the descriptors of corresponding keypoints in paired images are close in feature space. While this sparse keypoint supervision helps the model learn semantically meaningful descriptors for the annotated keypoints, it does not guarantee consistency for unlabeled regions of the object.

A promising direction to address this limitation is to incorporate 3D geometry by assigning each pixel a coordinate in an object centric reference frame. Prior works [42, 29] explores this idea by projecting object surfaces onto a spherical coordinate system, with each coordinate on the sphere corresponding to a different characteristic point of the object. However, this requires inferring both object shape and the viewpoint from a collection of 2D images, a highly ill-posed problem, which requires generating pairs through synthetic warps resulting unrealistic shapes [42] or relies on viewpoint supervision which can be challenging to predict automatically. Next we show how to combine sparse keypoints annotations with 3D geometry cues to learn dense, semantically consistent descriptors for every pixel in an image. An overview of our approach is shown in Fig. 2.

3.2 Canonical Representation Learning

Similar to [42, 29], we aim to learn a 3D *canonical* representation for each object category, along with a function $\varphi(I, \mathbf{u}) \rightarrow \mathbf{x} \in \mathbb{R}^3$ that maps a pixel \mathbf{u} in image I to its 3D coordinates in the canonical object-centric coordinate system. Unlike the spherical representations in prior work [42, 29], we do not impose any topological constraints on the canonical representation (e.g., enforcing a spherical surface). We parameterized the canonical representation by a set of 3D keypoints $\mathcal{P} = \{\mathbf{p}_1, \dots, \mathbf{p}_{|\mathcal{K}|}\}$, where each \mathbf{p}_i corresponds to a labeled keypoint \mathbf{k}_i in I . Crucially, \mathcal{P} is shared across all instances of a category, and is invariant to object instance, viewpoint, and pose, unlike \mathcal{K} , ensuring the canonicity of the representation.

To compute \mathcal{P} , we first compute the 3D coordinates of each keypoint \mathbf{k} in image I using a monocular depth model $\Psi(I, \mathbf{k}) \rightarrow \mathbb{R}^+$ and then backproject it by using estimated camera intrinsics $\mathbf{A} \in \mathbb{R}^{3 \times 3}$ as follows:

$$\bar{\mathbf{k}} = \Psi(I, \mathbf{k}) \mathbf{A}^{-1} [k_x, k_y, 1]^\top, \quad (2)$$

where $\mathbf{k} = (k_x, k_y)$ and $\bar{\mathbf{k}} \in \mathbb{R}^3$ represents the 3D ‘posed’ coordinate. We denote the set of backprojected coordinates as $\bar{\mathcal{K}} = \{\bar{\mathbf{k}}_1, \dots, \bar{\mathbf{k}}_{|\mathcal{K}|}\}$.

To align $\hat{\mathcal{K}}$ with \mathcal{P} , we compute a rigid transformation, comprising rotation $\mathbf{R} \in SO(3)$ and translation $\mathbf{T} \in \mathbb{R}^3$, and scale $s \in \mathbb{R}^+$ such that $\mathbf{M} = s[\mathbf{R}|\mathbf{T}] \in \mathbb{R}^{3 \times 4}$. We optimize the canonical keypoints \mathcal{P} by minimizing their alignment error across the training set using a nested optimization:

$$\min_{\mathbf{p}_i} \sum_{n=1}^N \|\mathbf{p}_i - \hat{\mathbf{M}}^{(n)} \bar{\mathbf{k}}_i^{(n)}\|_1 \quad \text{where} \quad \hat{\mathbf{M}}^{(n)} = \arg \min_{\mathbf{M}} \sum_{i=1}^{|\mathcal{K}|} \|\mathbf{p}_i - \mathbf{M} \bar{\mathbf{k}}_i^{(n)}\|_2. \quad (3)$$

In the inner loop, we use Kabsch’s algorithm [18] to efficiently compute the optimal rigid alignment $\hat{\mathbf{M}}^{(n)}$ between the canonical and posed coordinates. Even though alignments rely on only a sparse subset of visible keypoints per-image, we find this sufficient to recover a globally consistent arrangement of the \mathcal{P} .

Next we associate each canonical keypoint in \mathbf{p} with a learnable descriptor \mathbf{z} , forming a set $\mathcal{Z} = \{\mathbf{z}_1, \dots, \mathbf{z}_{|\mathcal{K}|}\}$. We learn these jointly with Φ , using a cross-entropy loss over cosine similarities between extracted and canonical descriptors:

$$\min_{\Phi, \mathcal{Z}} -\frac{1}{N} \sum_{n=1}^N \sum_{i=1}^{|\mathcal{K}|} \log \frac{\exp(\text{sim}(\mathbf{z}_i, \Phi(I^{(n)}, \mathbf{k}_i^{(n)}))/\tau)}{\sum_{j=1}^{|\mathcal{K}|} \exp(\text{sim}(\mathbf{z}_j, \Phi(I^{(n)}, \mathbf{k}_j^{(n)}))/\tau)}, \quad (4)$$

with cosine similarity $\text{sim}(\cdot, \cdot)$ and learned temperature parameter τ . This objective encourages Φ to produce distinctive and semantically consistent features across object instances for each keypoint \mathbf{k} .

3.3 Dense Geometric Alignment

So far, we have only modeled object geometry at the sparse level via \mathcal{P} . We now extend this to dense correspondence by defining $\varphi(I, \mathbf{u})$, a function that maps every pixel \mathbf{u} in I to a coordinate in the canonical space. We compute it as an attention-weighted sum over canonical keypoints:

$$\varphi(I, \mathbf{u}) = \sum_{i=1}^{|\mathcal{K}|} \frac{\exp(\text{sim}(\mathbf{z}_i, \Phi(I, \mathbf{u}))/\tau)}{\sum_{j=1}^{|\mathcal{K}|} \exp(\text{sim}(\mathbf{z}_j, \Phi(I, \mathbf{u}))/\tau)} \mathbf{p}_i. \quad (5)$$

This is equivalent to computing descriptors via softmax attention over \mathcal{Z} , using $\Phi(I, \mathbf{u})$ as queries, \mathbf{z} as keys, and \mathbf{p} as values. For labeled keypoints \mathbf{k}_l , minimizing Eq. (4) ensures $\varphi(I, \mathbf{k}_l) = \mathbf{p}_l$.

For each training image I , we can now estimate the dense canonical coordinates \mathcal{X}^c over its pixels via Eq. (5), and the posed coordinates \mathcal{X}^b via depth backprojection using Eq. (2). In practice, \mathcal{X}^c and \mathcal{X}^b only consist of object points that are selected using the segmentation mask. We aim to align these two representations so that \mathcal{X}^c properly reflects the object geometry. However, our annotations are only sparse, thus we cannot directly supervise $\varphi(I, \mathbf{u})$ for arbitrary coordinates \mathbf{u} . Instead, we make the assumption that even though the posed and canonical shape are different, they should be *locally* similar. We encourage the geometric alignment between a small neighborhood of points sampled in the posed space, and their corresponding locations in the canonical space.

For a given point $q \in \mathcal{X}^c$, we sample its k nearest neighbors to obtain \mathbf{C}_q in the canonical space, and the corresponding coordinates in the posed space \mathbf{B}_q , and minimize the alignment error between two sets. We also sample neighbors of a given point $r \in \mathcal{X}^b$ in the posed space, denoted as \mathbf{B}_r , and compute the loss in the other direction:

$$\min_{\Phi, \mathcal{Z}} \frac{1}{N} \sum_{n=1}^N \|\mathbf{C}_q^{(n)} - \mathbf{M}_{c2b}^{(n)} \mathbf{B}_q^{(n)}\|_1 + \|\mathbf{B}_r^{(n)} - \mathbf{M}_{b2c}^{(n)} \mathbf{C}_r^{(n)}\|_1, \quad (6)$$

where \mathbf{M}_{c2b} and \mathbf{M}_{b2c} are the rigid transformations between the canonical and posed coordinates, computed using Kabsch’s algorithm at each iteration as in Eq. (3).

In the canonical space, neighbors are selected using a standard k-nearest neighbors strategy. However, this approach can be unreliable in the posed space due to object deformations. For instance, in the case of a person eating, the hand might be close to the face in 3D space, and thus points belonging to the face might mistakenly be selected as neighbors of the hand. Instead, we use a geodesic sampling strategy, that samples points along the surface of the object. Starting from a seed point, we iteratively grow the neighborhood by selecting the next point with the shortest geodesic distance to the current set, effectively approximating surface-based proximity rather than raw spatial closeness.

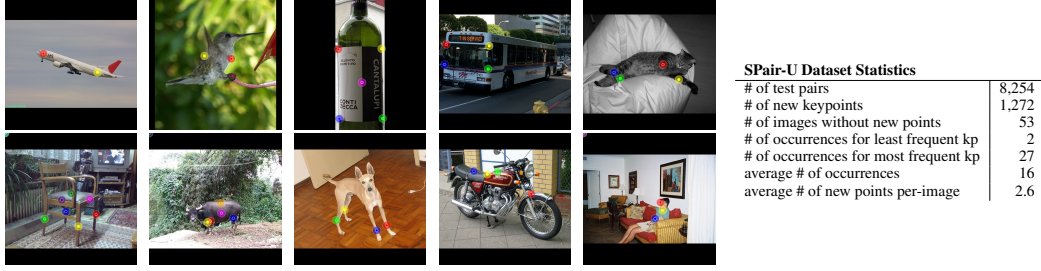


Figure 3: Example keypoint annotations contained within our new **SPair-U** evaluation dataset. It utilizes the same images as the SPair-71k dataset [30], but adds additional keypoints not present in SPair-71k. This enables benchmarking of SC methods on the existing keypoints along with our new ones. On the right we summarize the main statistics of our new dataset.

We jointly optimize the descriptor learning loss in Eq. (4) and the geometric consistency loss in Eq. (6) to learn Φ and \mathcal{P} . While these objectives suffice to learn an SC model, in practice we build our implementation on Geo-SC [54] and optimize its parameters jointly over the sum of our objective and the original one. At inference time, rather than simply querying nearest-neighbor in the descriptor space predicted by Φ , we make use of the soft-argmax window matching strategy proposed in [54]. Unlike φ , which relies on category-specific canonical coordinate set \mathcal{P} and descriptors \mathcal{Z} , Φ can be applied to previously unseen object categories directly.

4 SPair-U: A Benchmark for Evaluating Unseen Keypoints

As illustrated in Fig. 1, the performance of the state-of-the-art supervised SC methods [54, 53] degrades significantly when queried on keypoints that are not part of the training set. We posit that this is caused by models only learning strong representations for these specific points, while largely ignoring the remaining pixels. We would like to assess the performance of SC methods when evaluated on keypoints that were previously unseen (i.e., not in the labeled set) at training time. A possible solution is to use an existing dataset while splitting the annotations into two mutually exclusive sets of keypoints, seen and unseen, between training and evaluation. However, this strategy would reduce the supervision available, and require retraining previous techniques for evaluation.

Instead, we introduce a new evaluation benchmark, **SPair-U**, by labeling additional keypoints from the SPair-71k dataset [30]. We added at least four new points for each of the 18 categories found in SPair-71k. For animals, we focused on additional joints on the limbs, and for vehicles we added semantic parts that were not already labeled, e.g., windshield or fenders. Boats, bottles, potted plants, and tv monitors keypoints are not semantic *per se* in SPair-71k, but are rather spread around on the outline of the object. Thus, we added midway points between those already defined. In total, we add 1,272 new test keypoint annotations resulting in 8,254 new test pairs. We illustrate some of these new annotations in Fig. 3, and the full list with more details can be found in Appendix D. As shown in Fig. 1, current supervised methods tend to default to making predictions new training keypoint locations when predicting correspondences for the SPair-U keypoints.

5 Experimental Results

5.1 Implementation Details

Our 3D prototype design being independent from typical semantic correspondence architectures, we can add it as an additional objective on top of established models. Thus, we base our experiments on Geo-SC [54], strictly following provided hyperparameters, e.g., learning rate, batch size, optimizer, scheduler, epoch count, simply adding our additional loss terms and jointly optimizing \mathcal{P} and \mathcal{Z} alongside Geo-SC’s feature extractor Φ . In practice, Φ consists of additional bottleneck layers trained on top of frozen DINOv2 and SD backbones. We extract depth maps and camera intrinsics using MoGe [47], and use Segment Anything [21] to obtain segmentation masks. Additional implementation details are provided in Appendix A.

5.2 Quantitative Results

SPair-71k. We first compare our models to other SC approaches on the SPair-71k benchmark [30], which contains images from 18 categories. We use the standard $\text{PCK}@0.1_{\text{bbox}}$ which considers a

Table 1: **Results on standard evaluation keypoints for SPair-71k.** Per-image PCK@0.1_{bbox} scores are reported. In this table and the following: All models use the soft matching strategy described in [54] except those followed by *. Models with a dagger[†] benefit from AP-10K pretraining. Models in the \mathcal{K} category use keypoint supervision, while \mathcal{K} do not. Best results are **bolded** and second best are underlined.






















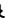







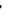




																		avg		
\mathcal{K} SD [37][53]	62.8	52.7	80.6	31.2	43.4	39.1	35.6	76.0	32.0	67.6	50.9	59.7	51.0	47.3	48.6	43.8	61.8	52.9	52.0	
	DINOv2 [35][53]	73.4	60.2	88.8	43.2	41.1	46.7	45.1	75.0	33.4	69.8	66.1	69.6	60.7	66.6	30.7	61.3	54.2	23.9	55.3
	DINOv2+SD [53]	73.8	61.0	89.6	40.2	52.5	47.4	44.1	81.1	41.5	76.8	64.8	70.5	61.7	66.3	54.3	62.7	63.5	52.4	61.1
	SphericalMaps [29]	76.2	60.1	90.0	46.5	53.0	74.9	68.0	83.8	45.1	81.7	67.6	75.4	69.1	58.9	50.0	67.5	73.9	58.1	66.1
\mathcal{K} SCorSan* [17]	57.1	40.3	78.3	38.1	51.8	57.8	47.1	67.9	25.2	71.3	63.9	49.3	45.3	49.8	48.8	40.3	77.7	69.7	55.3	
	CATS++* [9]	60.6	46.9	82.5	41.6	56.8	64.9	50.4	72.8	29.2	75.8	65.4	62.5	50.9	56.1	54.8	48.2	80.9	74.9	59.8
	DHF* [28]	74.0	61.0	87.2	40.7	47.8	70.0	74.4	80.9	38.5	76.1	60.9	66.8	66.6	70.3	58.0	54.3	87.4	60.3	64.9
	DINO+SD (S) [53]	84.7	67.5	93.2	64.5	59.2	85.7	82.0	89.8	57.0	89.3	76.2	80.8	75.9	80.2	64.7	71.2	93.6	70.5	76.5
	Geo-SC [54]	86.6	70.7	95.8	69.2	64.8	94.5	90.6	91.0	67.1	91.8	86.1	86.3	79.3	87.9	80.8	82.1	96.6	83.4	83.2
	Geo-SC [†] [54]	92.0	76.1	97.2	70.4	70.5	91.4	89.7	92.7	73.4	95.0	90.5	87.7	81.8	91.6	82.3	83.4	96.5	85.3	85.6
	Ours	86.8	72.6	95.3	70.7	64.8	94.6	90.3	89.4	70.7	94.1	84.8	83.0	80.5	87.0	79.1	77.5	95.8	82.8	82.9
	Ours [†]	92.2	76.3	96.5	72.0	68.1	95.0	90.8	93.1	75.1	94.2	91.2	86.0	82.1	91.7	80.0	81.2	95.8	84.0	85.4

Table 2: **Results on unseen keypoints on our SPair-U benchmark.** Per-image PCK@0.1_{bbox} scores on unseen keypoints are reported.

																		avg	
\mathcal{K} SD [37][53]	73.2	71.8	48.8	37.7	43.0	55.1	47.2	25.4	35.9	60.4	46.2	41.6	59.9	53.1	57.8	36.1	50.6	19.5	47.4
DINOv2 [35][53]	88.2	75.6	79.0	52.9	39.8	54.1	60.0	43.9	34.8	67.2	64.6	53.6	75.8	<u>79.1</u>	37.8	45.6	<u>53.3</u>	8.4	54.9
DINOv2+SD [53]	88.0	80.4	<u>72.3</u>	48.2	47.9	62.3	61.5	44.8	45.0	<u>73.0</u>	64.7	58.2	75.5	80.0	62.7	46.1	55.9	16.9	59.4
SphericalMaps [29]	90.2	<u>76.8</u>	71.7	55.6	<u>44.6</u>	89.5	81.7	50.8	<u>46.4</u>	71.2	70.4	62.9	65.4	68.2	56.1	45.9	51.6	26.9	61.0
\mathcal{K} SCorSan* [17]	56.9	26.9	23.0	37.6	31.4	52.8	41.7	16.6	15.4	21.0	47.1	17.8	27.3	48.1	47.8	20.1	28.0	34.2	32.7
CATS++* [9]	69.9	43.8	14.0	47.1	31.9	69.5	47.0	11.7	24.4	15.1	47.9	25.8	32.0	54.3	51.6	17.5	27.9	22.8	35.9
DHF* [28]	71.4	58.1	39.1	35.8	44.7	74.0	40.2	33.5	27.4	52.0	50.4	41.6	56.5	51.6	41.6	30.0	42.5	14.5	43.3
DINO+SD (S) [53]	81.5	73.6	57.1	63.4	35.8	85.7	67.7	64.3	39.3	67.9	86.8	79.5	60.9	70.1	55.8	57.8	42.7	12.6	60.0
Geo-SC [54]	80.9	71.4	51.8	65.3	36.9	91.0	70.8	55.7	36.9	55.7	79.2	53.7	66.5	62.3	61.1	39.0	39.0	17.4	56.9
Geo-SC [†] [54]	74.6	70.6	55.5	65.1	36.4	85.1	72.3	50.1	40.1	60.6	85.3	65.7	52.9	61.9	66.6	41.8	36.6	13.8	57.1
Ours	80.3	74.5	70.6	<u>67.1</u>	40.2	92.9	72.7	53.8	45.8	68.5	75.3	62.0	67.8	65.4	<u>68.1</u>	45.4	47.9	30.5	<u>62.4</u>
Ours [†]	81.1	73.2	72.0	67.5	35.2	<u>92.1</u>	<u>75.5</u>	<u>61.2</u>	51.4	74.3	86.8	<u>78.8</u>	70.9	68.9	72.6	<u>54.7</u>	44.8	<u>32.2</u>	66.1

match to be correct if its prediction lies within distance $0.1 \times \max(h, w)$ of the ground truth location where (h, w) is the height and width of the target object bounding box. Typically, supervised models report *per-image* PCK, i.e., the average score of each image per category, while unsupervised ones use *per point* PCK, i.e., the average number of correct matches per category. In order to properly compare performances between the two families, we recompute *per-image* PCK for all models, which results in a small drop for the unsupervised models.

Results in Table 1 show that our model ranks competitively against other approaches, with a marginal 0.2% performance drop on average against its backbone Geo-SC [54]. Per category results show small improvements in 9 of the categories, the highest one being 3.6% on bus, and small drop on the other 9, the largest being 2.4% on bottle. Overall, the differences are minor, illustrating that adding our extra objective does not interfere with the original model.

SPair-U. To evaluate the model’s ability to generalize to unseen semantic points, we assess its performance on the introduced SPair-U keypoints using per-image PCK@0.1_{bbox} for a like-for-like comparison. We exclude the Test-time Adaptive Pose Alignment from [54] since it requires prior knowledge of keypoint semantics to relabel flipped keypoints, which contradicts the assumption that evaluation keypoints are unknown.

As shown in Table 2, results on SPair-U reveal a stark contrast between supervised and unsupervised models. While unsupervised models see only a modest performance drop, likely due to increased task difficulty, supervised models experience a significant decline. Many of the pre-existing approaches are outperformed by the unsupervised DINO+SD baseline [53] and they are consistently beaten by the weakly-supervised Spherical Maps [29]. Notably, in 8 categories, the best-performing model is unsupervised, suggesting that supervised approaches behave more like keypoint regressors and fail to generalize to novel correspondences.

Our method also shows some performance degradation on SPair-U, but the drop is smaller than that of its backbone Geo-SC. It achieves the highest overall performance, improving upon the best prior supervised model by 6.1%, indicating stronger generalization to unseen keypoints. Nevertheless, the substantial gap between results on SPair-71k and SPair-U underscores a broader limitation: despite recent progress, most models struggle to move beyond sparse keypoint supervision toward robust, general semantic correspondence.

Cross-benchmark evaluation. We further evaluate our model on four benchmarks: SPair-71k, SPair-U, AP-10k [54], and PF-PASCAL [14]. While most supervised SC methods train separate

Table 3: **Cross-benchmark evaluation on held-out datasets.** Scores are reported using PCK with different thresholds. Here, only keypoint supervision from Spair-71k is used for supervised models.

PCK threshold	Spair-71k			Spair-U			AP-10K IS			AP-10K CS			AP-10K CF			PF-PASCAL		
	0.01	0.05	0.10	0.01	0.05	0.10	0.01	0.05	0.10	0.01	0.05	0.10	0.01	0.05	0.10	0.05	0.10	0.15
\mathcal{K} SD [37][53]	6.3	37.3	52.0	3.3	28.0	47.4	8.4	36.9	52.5	6.6	32.6	47.9	4.3	24.6	37.6	66.1	80.0	85.3
DINOv2 [35][53]	6.8	38.0	55.3	3.7	32.4	54.9	10.5	44.8	63.6	8.8	41.7	61.6	7.7	34.7	52.0	62.4	78.2	83.5
DINOv2+SD [53]	8.2	44.2	61.1	4.7	37.0	59.4	11.7	47.4	65.8	10.0	44.0	63.5	7.7	35.4	52.4	72.5	85.6	90.3
SphericalMaps [29]	8.2	47.7	66.1	4.5	38.2	<u>61.0</u>	12.5	48.5	66.7	10.6	44.9	63.6	8.0	35.7	52.1	74.6	88.9	93.2
\mathcal{K} DINO+SD (S) [53]	13.0	61.6	76.5	3.6	35.9	59.3	15.1	54.3	71.7	13.6	51.1	<u>68.7</u>	11.0	44.0	<u>60.4</u>	74.5	87.4	91.1
Geo-SC [54]	<u>20.0</u>	72.2	83.2	<u>4.6</u>	35.5	56.9	16.6	55.8	70.5	15.2	<u>52.4</u>	67.7	11.9	<u>45.9</u>	59.6	<u>75.3</u>	87.0	90.7
Ours	20.5	<u>72.1</u>	<u>82.9</u>	4.2	<u>37.8</u>	62.4	<u>16.5</u>	55.8	<u>71.3</u>	<u>15.1</u>	53.0	69.0	<u>11.2</u>	46.1	61.1	75.8	<u>87.5</u>	<u>91.2</u>

models for each benchmark, this setup encourages overfitting to the benchmark and is impractical for real-world use. Instead, we advocate for evaluating generalization by training a single model on one dataset and testing it across multiple benchmarks. We choose SPair-71k for training due to its balanced mix of object and animal categories, making it suitable for generalization. To ensure fairness, we exclude models pretrained on AP-10K and standardize evaluation using the windowed soft-argmax protocol from [54].

As shown in Table 3, while Geo-SC [54] achieves the best performance on the standard SPair-71k test set, it underperforms on all other benchmarks, highlighting its limited generalization. Notably, even a simple supervised DINO+SD [53] baseline outperforms Geo-SC at the standard 0.10 threshold when using the same soft window matching strategy. This stands in sharp contrast to the findings in [54] where Geo-SC consistently outperforms its baseline by 10% on the 3 AP-10K benchmarks, when both models are trained on AP-10K, indicating potential overfitting to that dataset.

Consistent with earlier observations, a clear pattern emerges: models trained without keypoint supervision maintain stable rankings and performance gaps across datasets, whereas supervised models cluster more tightly in performance when evaluated out of their training distribution, revealing weaker cross-set generalization.

5.3 Qualitative Results

In Fig. 4, we visualize Principal Component Analysis of object features produced by our model, Geo-SC and the unsupervised DINO+SD. Our model produces descriptors that vary smoothly over the object surface while uniquely identifying each point. In comparison, the predictions of Geo-SC are noisier, with sudden discontinuities (cf. bus) and uniform descriptors on regions that have no keypoints (cf. the body of the cat and the cow). Meanwhile, the unsupervised features fail to separate repeated parts (cf. plane engines) and produces noisy features in textureless areas (cf. tv).

Following [45], we visualize our learned canonical shapes in Fig. 5 by randomly logging predicted canonical coordinates of objects in order to overlap multiple partial point clouds over the training data. We observe that the spatial organization of \mathcal{P} , i.e., the large bold points, captures the general

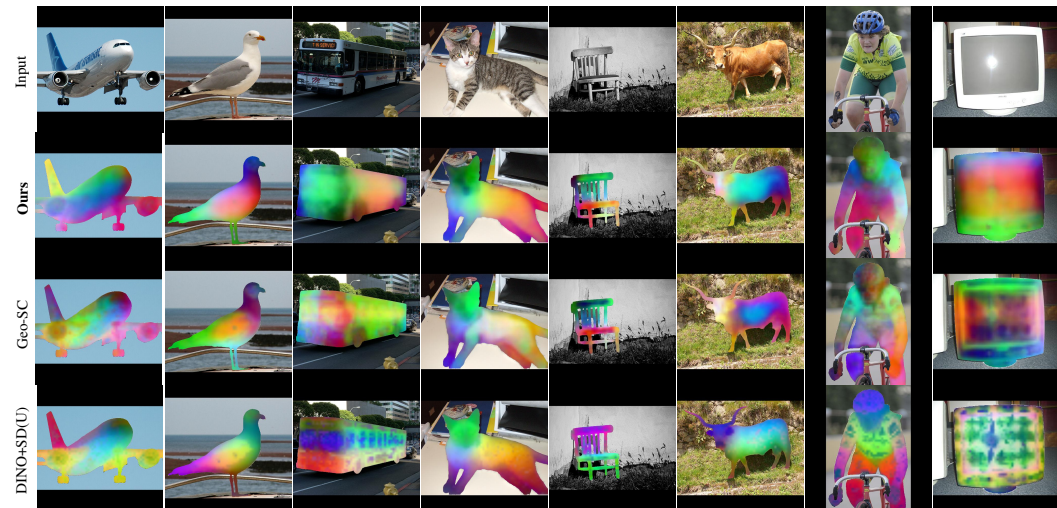


Figure 4: PCA decomposition of the feature maps for different models. Note that PCA is computed on object features only. The inclusion of geometric constraints during training results in fewer high frequency artifacts in the predicted feature maps for our approach.

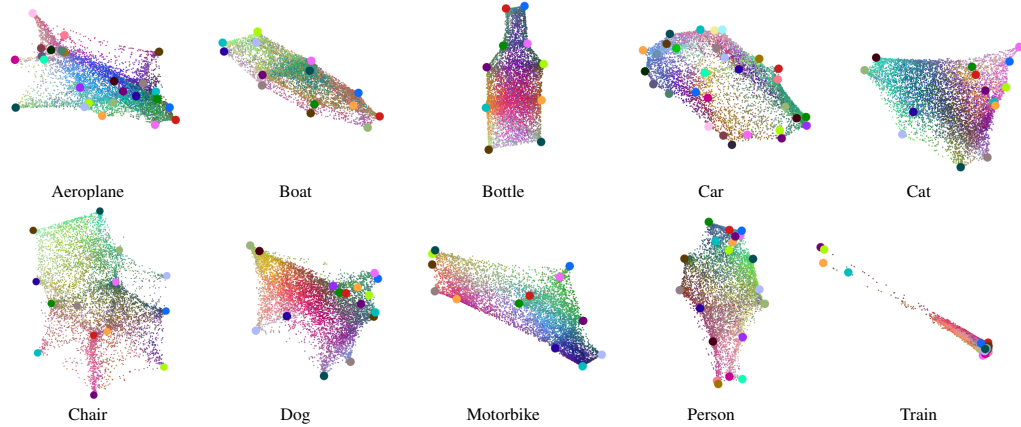


Figure 5: **Visualization of our learned canonical shapes.** Large points correspond to \mathcal{P} , each being attributed a distinctive color for visualization. Small points are predicted canonical coordinates of objects, colored with PCA of the features predicted by φ .

shape of the category, and the predicted coordinates densely span the object surface. Interestingly, our parametrization of the canonical shape Eq. (5) forces predicted coordinates to lie within the convex hull of \mathcal{P} , which explains the incomplete wheel on the motorbike. We also observe that very few points are mapped towards the end of the train, which we attribute to the varying length of trains across instances and the bias toward frontal viewpoints. Note that contrary to [45], these are simply visualizations and are not used for inference, meaning this limitation is unlikely to significantly affect performance.

6 Limitations

While augmenting the test set of SPair-71k with new keypoints enables us to evaluate existing techniques with their provided models and code, our proposed benchmark SPair-U inherits some drawbacks from SPair-71k. In particular, the test set is small, consisting of only 481 images but with over 8,000 test pairs, and the categories are restricted to only common objects and animals. Furthermore, few categories were already labeled with a high number of keypoints where it is potentially easier to detect the newly added ones by relating them to the existing ones. While our findings remain valid about the generalization issues in supervised SC techniques, a larger, higher-quality held-out set of images and points would be beneficial for more extensive evaluation.

Compared to prior supervised methods [17, 8, 28, 54], our approach incorporates additional supervision in the form of depth maps and segmentation masks, similar to [45], although in our case, they are only used during training. Furthermore, unlike [29], which relies on camera viewpoint annotations that off-the-shelf models cannot reliably provide, we obtain all additional signals using existing pretrained models.

Finally, our assumption that geometry is a good proxy for semantics breaks down for complex object categories with diverse spatial part configurations. For example, cabinets may have different numbers of doors that open in various directions, leading to inconsistent placement of features like handles. Additionally, we do not foresee any negative social impacts of our work.

7 Conclusion

We tackled the problem of estimating semantic correspondences between different instances of the same object category. While recent supervised methods have made significant progress on known keypoints, we showed that their representations often fail to generalize to unseen keypoints not annotated during training. To address this limitation, we proposed a new approach that incorporates geometric constraints at training time through a per-category, learned continuous canonical manifold. Our method achieves superior performance compared to both supervised and unsupervised baselines, as demonstrated on SPair-U, a new dataset we introduce with additional keypoint annotations for the widely used SPair-71k benchmark.

Acknowledgments. This project was supported by the EPSRC Visual AI grant EP/T028572/1.

References

- [1] Shir Amir, Yossi Gandelsman, Shai Bagon, and Tali Dekel. Deep vit features as dense visual descriptors. *ECCV Workshops*, 2022.
- [2] Mehmet Aygün and Oisin Mac Aodha. Demystifying unsupervised semantic correspondence estimation. In *ECCV*, 2022.
- [3] Mehmet Aygün and Oisin Mac Aodha. SAOR: Single-View Articulated Object Reconstruction. In *CVPR*, 2024.
- [4] Nir Barel, Ron Shapira Weber, Nir Mualeem, Shahaf E Finder, and Oren Freifeld. Spacejam: a lightweight and regularization-free method for fast joint alignment of images. In *ECCV*, 2024.
- [5] Shariq Farooq Bhat, Reiner Birkel, Diana Wofk, Peter Wonka, and Matthias Müller. Zoedepth: Zero-shot transfer by combining relative and metric depth, 2023.
- [6] Mathilde Caron, Hugo Touvron, Ishan Misra, Hervé Jégou, Julien Mairal, Piotr Bojanowski, and Armand Joulin. Emerging properties in self-supervised vision transformers. In *ICCV*, 2021.
- [7] Xinle Cheng, Congyue Deng, Adam W Harley, Yixin Zhu, and Leonidas Guibas. Zero-shot image feature consensus with deep functional maps. In *ECCV*, 2024.
- [8] Seokju Cho, Sunghwan Hong, Sangryul Jeon, Yunsung Lee, Kwanghoon Sohn, and Seungryong Kim. Cats: Cost aggregation transformers for visual correspondence. *NeurIPS*, 2021.
- [9] Seokju Cho, Sunghwan Hong, and Seungryong Kim. Cats++: Boosting cost aggregation with convolutions and transformers. *PAMI*, 2022.
- [10] Andrew J Davison, Ian D Reid, Nicholas D Molton, and Olivier Stasse. Monoslam: Real-time single camera slam. *PAMI*, 2007.
- [11] Abhishek Dutta and Andrew Zisserman. The VIA annotation software for images, audio and video. In *International Conference on Multimedia*, 2019.
- [12] Xiao Fu, Wei Yin, Mu Hu, Kaixuan Wang, Yuexin Ma, Ping Tan, Shaojie Shen, Dahua Lin, and Xiaoxiao Long. Geowizard: Unleashing the diffusion priors for 3d geometry estimation from a single image. In *ECCV*, 2024.
- [13] Kamal Gupta, Varun Jampani, Carlos Esteves, Abhinav Shrivastava, Ameesh Makadia, Noah Snavely, and Abhishek Kar. Asic: Aligning sparse in-the-wild image collections. In *ICCV*, 2023.
- [14] Bumsu Ham, Minsu Cho, Cordelia Schmid, and Jean Ponce. Proposal flow: Semantic correspondences from object proposals. *PAMI*, 2017.
- [15] Kai Han, Rafael S Rezende, Bumsu Ham, Kwan-Yee K Wong, Minsu Cho, Cordelia Schmid, and Jean Ponce. Snet: Learning semantic correspondence. In *ICCV*, 2017.
- [16] Or Hirschorn and Shai Avidan. A graph-based approach for category-agnostic pose estimation. In *ECCV*, 2024.
- [17] Shuaiyi Huang, Luyu Yang, Bo He, Songyang Zhang, Xuming He, and Abhinav Shrivastava. Learning semantic correspondence with sparse annotations. In *ECCV*, 2022.
- [18] Wolfgang Kabsch. A solution for the best rotation to relate two sets of vectors. *Foundations of Crystallography*, 1976.
- [19] Angjoo Kanazawa, David W Jacobs, and Manmohan Chandraker. Warpnet: Weakly supervised matching for single-view reconstruction. In *CVPR*, 2016.
- [20] Bingxin Ke, Anton Obukhov, Shengyu Huang, Nando Metzger, Rodrigo Caye Daudt, and Konrad Schindler. Repurposing diffusion-based image generators for monocular depth estimation. In *CVPR*, 2024.

- [21] Alexander Kirillov, Eric Mintun, Nikhila Ravi, Hanzi Mao, Chloe Rolland, Laura Gustafson, Tete Xiao, Spencer Whitehead, Alexander C Berg, Wan-Yen Lo, et al. Segment anything. In *ICCV*, 2023.
- [22] Nilesh Kulkarni, Abhinav Gupta, and Shubham Tulsiani. Canonical surface mapping via geometric cycle consistency. In *ICCV*, 2019.
- [23] Ce Liu, Jenny Yuen, and Antonio Torralba. Sift flow: Dense correspondence across scenes and its applications. *PAMI*, 2010.
- [24] Ilya Loshchilov and Frank Hutter. Decoupled weight decay regularization. In *ICLR*, 2019.
- [25] Changsheng Lu and Piotr Koniusz. Few-shot keypoint detection with uncertainty learning for unseen species. In *CVPR*, 2022.
- [26] Changsheng Lu and Piotr Koniusz. Detect any keypoints: An efficient light-weight few-shot keypoint detector. In *AAAI*, 2024.
- [27] Changsheng Lu, Zheyuan Liu, and Piotr Koniusz. Openkd: Opening prompt diversity for zero-and few-shot keypoint detection. In *ECCV*, 2024.
- [28] Grace Luo, Lisa Dunlap, Dong Huk Park, Aleksander Holynski, and Trevor Darrell. Diffusion hyperfeatures: Searching through time and space for semantic correspondence. *NeurIPS*, 2023.
- [29] Octave Mariotti, Oisin Mac Aodha, and Hakan Bilen. Improving semantic correspondence with viewpoint-guided spherical maps. In *CVPR*, 2024.
- [30] Juhong Min, Jongmin Lee, Jean Ponce, and Minsu Cho. Spair-71k: A large-scale benchmark for semantic correspondence. *arXiv:1908.10543*, 2019.
- [31] Juhong Min, Jongmin Lee, Jean Ponce, and Minsu Cho. Learning to compose hypercolumns for visual correspondence. In *ECCV*, 2020.
- [32] Tom Monnier, Matthew Fisher, Alexei A Efros, and Mathieu Aubry. Share with thy neighbors: Single-view reconstruction by cross-instance consistency. In *ECCV*, 2022.
- [33] Natalia Neverova, David Novotny, Marc Szafraniec, Vasil Khalidov, Patrick Labatut, and Andrea Vedaldi. Continuous surface embeddings. In *NeurIPS*, 2020.
- [34] Dolev Ofri-Amar, Michal Geyer, Yoni Kasten, and Tali Dekel. Neural congealing: Aligning images to a joint semantic atlas. In *CVPR*, 2023.
- [35] Maxime Oquab, Timothée Darcet, Théo Moutakanni, Huy Vo, Marc Szafraniec, Vasil Khalidov, Pierre Fernandez, Daniel Haziza, Francisco Massa, Alaaeldin El-Nouby, et al. Dinov2: Learning robust visual features without supervision. *TMLR*, 2024.
- [36] René Ranftl, Katrin Lasinger, David Hafner, Konrad Schindler, and Vladlen Koltun. Towards robust monocular depth estimation: Mixing datasets for zero-shot cross-dataset transfer. *PAMI*, 2020.
- [37] Robin Rombach, Andreas Blattmann, Dominik Lorenz, Patrick Esser, and Björn Ommer. High-resolution image synthesis with latent diffusion models. In *CVPR*, 2022.
- [38] Johannes L Schonberger and Jan-Michael Frahm. Structure-from-motion revisited. In *CVPR*, 2016.
- [39] Leslie N Smith and Nicholay Topin. Super-convergence: Very fast training of neural networks using large learning rates. In *Artificial intelligence and machine learning for multi-domain operations applications*, 2019.
- [40] Luming Tang, Menglin Jia, Qianqian Wang, Cheng Perng Phoo, and Bharath Hariharan. Emergent correspondence from image diffusion. In *NeurIPS*, 2023.
- [41] James Thewlis, Samuel Albanie, Hakan Bilen, and Andrea Vedaldi. Unsupervised learning of landmarks by descriptor vector exchange. In *ICCV*, 2019.

- [42] James Thewlis, Hakan Bilen, and Andrea Vedaldi. Unsupervised learning of object frames by dense equivariant image labelling. *NeurIPS*, 2017.
- [43] Nikolaos Tsagkas, Jack Rome, Subramanian Ramamoorthy, Oisin Mac Aodha, and Chris Xiaoxuan Lu. Click to grasp: Zero-shot precise manipulation via visual diffusion descriptors. In *IROS*, 2024.
- [44] C. Wah, S. Branson, P. Welinder, P. Perona, and S. Belongie. The caltech-ucsd birds-200-2011 dataset, 2011.
- [45] Krispin Wandell and Hesheng Wang. Semalign3d: Semantic correspondence between rgb-images through aligning 3d object-class representations. *arXiv:2503.22462*, 2025.
- [46] Qianqian Wang, Yen-Yu Chang, Ruojin Cai, Zhengqi Li, Bharath Hariharan, Aleksander Holynski, and Noah Snavely. Tracking everything everywhere all at once. In *ICCV*, 2023.
- [47] Ruicheng Wang, Sicheng Xu, Cassie Dai, Jianfeng Xiang, Yu Deng, Xin Tong, and Jiaolong Yang. Moge: Unlocking accurate monocular geometry estimation for open-domain images with optimal training supervision. *arXiv:2410.19115*, 2024.
- [48] Shuzhe Wang, Vincent Leroy, Yohann Cabon, Boris Chidlovskii, and Jerome Revaud. Dust3r: Geometric 3d vision made easy. In *CVPR*, 2024.
- [49] Shangzhe Wu, Ruining Li, Tomas Jakab, Christian Rupprecht, and Andrea Vedaldi. MagicPony: Learning articulated 3d animals in the wild. In *ICCV*, 2023.
- [50] Yuxi Xiao, Qianqian Wang, Shangzhan Zhang, Nan Xue, Sida Peng, Yujun Shen, and Xiaowei Zhou. Spatialtracker: Tracking any 2d pixels in 3d space. In *CVPR*, 2024.
- [51] Lihe Yang, Bingyi Kang, Zilong Huang, Zhen Zhao, Xiaogang Xu, Jiashi Feng, and Hengshuang Zhao. Depth anything v2. *NeurIPS*, 2024.
- [52] Hao Zhang, Lumin Xu, Shenqi Lai, Wenqi Shao, Nanning Zheng, Ping Luo, Yu Qiao, and Kaipeng Zhang. Open-vocabulary animal keypoint detection with semantic-feature matching. *IJCV*, 2024.
- [53] Junyi Zhang, Charles Herrmann, Junhwa Hur, Luisa Polania Cabrera, Varun Jampani, Deqing Sun, and Ming-Hsuan Yang. A tale of two features: Stable diffusion complements dino for zero-shot semantic correspondence. In *NeurIPS*, 2023.
- [54] Junyi Zhang, Charles Herrmann, Junhwa Hur, Eric Chen, Varun Jampani, Deqing Sun, and Ming-Hsuan Yang. Telling left from right: Identifying geometry-aware semantic correspondence. In *CVPR*, 2024.
- [55] Xu Zhang, Wen Wang, Zhe Chen, Yufei Xu, Jing Zhang, and Dacheng Tao. Clamp: Prompt-based contrastive learning for connecting language and animal pose. In *CVPR*, 2023.
- [56] Tinghui Zhou, Philipp Krahenbuhl, Mathieu Aubry, Qixing Huang, and Alexei A Efros. Learning dense correspondence via 3d-guided cycle consistency. In *CVPR*, 2016.

Appendix

A Additional Implementation Details

We base our model on Geo-SC [54], reusing all default hyperparameters that come with the official implementation¹, e.g., training for 2 epochs using AdamW [24] optimizer with 1.25×10^{-3} initial learning rate and 1.0×10^{-3} weight decay, coupled with one-cycle learning rate scheduler [39], with a batch size of 1. Every 5,000 iterations, models are evaluated on the validation split, and the best performing model is retained. For evaluation, unless stated otherwise, a soft-argmax window of size 15 is used.

Geo-SC specific hyperparameters are also untouched, with the contrastive $\mathcal{L}_{\text{sparse}}$ and dense $\mathcal{L}_{\text{dense}}$ objectives with gaussian noise being used, as well as feature maps dropout and pose-variant augmentation. We refer to the original publication and official implementation for in-depth description of these features.

Our complete loss term is $\mathcal{L}_{\text{sparse}} + \mathcal{L}_{\text{dense}} + \mathcal{L}_{\mathcal{P}} + 0.3 \times \mathcal{L}_{\mathcal{Z}} + \mathcal{L}_{\text{geom}}$, where $\mathcal{L}_{\mathcal{P}}$, $\mathcal{L}_{\mathcal{Z}}$, and $\mathcal{L}_{\text{geom}}$ correspond to Eq. (3), Eq. (4) and Eq. (6) respectively. The justification for setting the weight $\lambda_{\mathcal{Z}} = 0.3$ is provided in Appendix B.

Experiments were performed on a single NVIDIA RTX 6000 Ada Generation, using pre-extracted DINOv2 and SD feature maps, depth maps, and segmentation masks. Training a model on SPair-71k consumes roughly 4.3GB of VRAM over 8 hours, representing an increased memory cost over Geo-SC’s 2.9GB, mainly due to the many \mathcal{X}_b and \mathcal{X}_c we sample, and a doubling of runtime from roughly 4 hours. At inference time however, there is no impact as we estimate matches using features predicted with Φ in the exact same way Geo-SC does.

B Ablations

Table A1: Average PCK@0.1 on SPair-71k validation set for different ablations.

$\lambda_{\mathcal{Z}} = 1$	85.9
$\lambda_{\mathcal{Z}} = 0.1$	86.1
K-nn sampling	85.9
Geodesic sampling	86.2
Full model	86.5

We perform ablations of our designs in Table A1, and report results on the the SPair-71k [30] validation set which helps us chose the best performing model. It is not possible to ablate individual loss terms as they each have a distinct purpose without which the prototype cannot properly be learned: $\mathcal{L}_{\mathcal{P}}$ optimizes \mathcal{P} , $\mathcal{L}_{\mathcal{Z}}$ optimizes \mathcal{Z} , and $\mathcal{L}_{\text{geom}}$ provides a dense supervision signal, i.e., a loss for $\Phi(I, \mathbf{u})$ when \mathbf{u} is an arbitrary object pixel, i.e., not a keypoint.

We show that setting $\lambda_{\mathcal{Z}}$ to 1 or 0.1 both negatively affect performance. We believe this is due to the interaction between $\mathcal{L}_{\mathcal{Z}}$ and $\mathcal{L}_{\text{geom}}$, as a high $\lambda_{\mathcal{Z}}$ would push Φ to collapse towards defaulting to predicting keypoint features \mathcal{Z} for most points, while a weight too low prevents correct prediction on the keypoints. We also test different neighbor sampling strategies for \mathcal{X}_b and \mathcal{X}_c , and show that sampling both spaces with either K-nearest neighbor or geodesic sampling is ineffective.

C Additional Results

C.1 Additional Metrics

Multiple recent works pointed out issues with evaluating using PCK, and proposed additional evaluation metrics to address its limitations.

PCK[†] [2] PCK matches are counted correct even if the prediction lies closer to a keypoint that is not the target, which can lead to high scores when many points are grouped together, even though the system does not distinguish between them. The authors introduce PCK[†] which only considers a match correct if it lies within the threshold *and* its closest annotated point is the target.

KAP [29] PCK only considers matches when both ground-truth points are visible and does not penalize systems that predict strong similarities for points that do not correspond, for instance

¹<https://github.com/Junyi42/geoaware-sc>

Table A2: **Evaluation under robust metrics.** All metrics use *per image* averaging, and all models use window soft-argmax. All models are trained on SPair-71k, and models with a double dagger[‡] benefit from AP-10K pretraining. Models in the \mathcal{K} category use keypoint supervision, while \mathcal{K} do not. Best results are **bolded** and second best are underlined.

Threshold	Spair-71k KAP			Spair-U KAP			Spair-71k PCK [†]			Spair-U PCK [†]			Spair-71k GA			AP-10K IS GA		
	0.01	0.05	0.10	0.01	0.05	0.10	0.01	0.05	0.10	0.01	0.05	0.10	0.01	0.05	0.10	0.01	0.05	0.10
\mathcal{K} SD [37][53]	38.2	47.5	53.0	43.4	51.6	58.5	6.3	34.4	44.4	3.3	27.7	45.4	4.2	28.3	43.3	1.3	15.3	31.0
DINOv2 [35][53]	37.8	47.1	52.8	43.3	52.4	60.6	6.7	34.4	46.0	3.7	32.1	52.1	3.6	26.3	43.4	2.3	25.6	47.0
DINOv2+SD [53]	38.4	49.6	55.9	43.7	54.2	62.8	8.1	41.0	52.8	4.7	36.6	56.6	4.8	32.7	50.8	2.4	26.1	48.1
SphericalMaps [29]	38.9	51.2	58.2	44.3	<u>55.4</u>	64.2	8.8	44.4	57.3	4.5	<u>37.8</u>	58.5	5.6	37.7	58.1	2.6	28.4	51.8
\mathcal{K} DINO+SD (S) [53]	39.1	55.4	64.1	43.8	54.7	63.9	13.0	59.7	72.0	3.6	35.5	57.2	10.2	53.6	69.7	2.8	32.1	56.6
Geo-SC [54]	39.8	59.3	67.8	43.8	54.2	62.8	20.0	69.8	78.3	<u>4.6</u>	35.1	54.9	17.2	65.6	78.0	3.7	33.6	<u>55.3</u>
Geo-SC [‡] [54]	40.1	61.0	69.2	43.8	54.1	62.8	22.0	73.0	80.9	4.3	35.8	55.3	20.0	70.9	<u>82.3</u>	-	-	-
Ours	39.8	59.8	68.1	44.0	55.0	<u>64.5</u>	20.4	69.8	78.1	4.2	37.4	<u>60.3</u>	17.4	65.8	<u>77.7</u>	<u>3.5</u>	<u>33.5</u>	56.1
Ours [‡]	<u>40.0</u>	<u>60.3</u>	<u>69.0</u>	<u>44.2</u>	56.0	66.0	<u>20.8</u>	<u>72.1</u>	<u>80.7</u>	4.5	41.3	64.2	<u>18.8</u>	<u>70.7</u>	82.4	-	-	-

between the two opposite sides of a car. KAP reformulate the correspondence evaluation as a binary classification problem between the pixels that are close to the target and those those that are not. Crucially, it penalizes high predictions when a source keypoint is invisible in the target.

Geo-aware subset (GA) [54] Finally, [2],[54] and [29] noted that SC pipelines - especially unsupervised ones - often make mistakes because of repeated parts and object symmetries. [54] proposed evaluation on the *Geo-aware* subset of points only, e.g., the points for which there is a symmetric corresponding point.

Results in Table A2 confirm the patterns observed in Section 5.2. For all metrics, supervised models performances drop back down to unsupervised-level or worse when evaluated outside their training labels. Interestingly, KAP scores do not widely vary between supervised and unsupervised models, indicating that supervised models are still likely to predict strong similarity between points when none exists.

C.2 Additional Visualizations

We visualize more canonical surfaces in Fig. A1. While the shapes are sensible, we observe some limitations in adequately modeling categories with extreme deformations like birds: points belonging to the wings are predicted close to the body when they are folded, and away when they are spread. However, this is consistent with SPair-71k labeling, where the tips are only labeled when the wings are spread.

We also show some predictions for the unsupervised DINOv2+SD, Geo-SC, and our model on SPair-U in Fig. A3. We observe some interesting failure cases: on the aeroplane, the unsupervised model

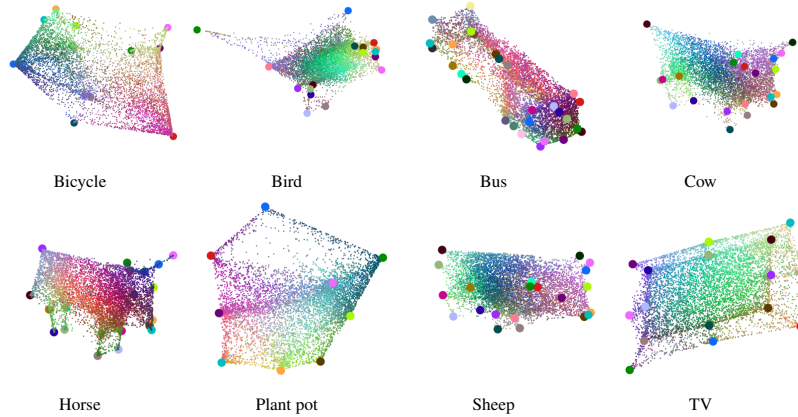


Figure A1: **Visualization of extra canonical shapes.** Large points correspond to \mathcal{P} , each being attributed a distinctive color for visualization. Small points are predicted canonical coordinates of objects, colored with PCA of the features predicted by φ .

correctly matches the door, while both supervised models incorrectly predict a training keypoint. In two occasions, Geo-SC predicts points outside of the object when queried on points that are far from training annotations (cow and person). Finally, two very challenging cases are shown with the chair and the tv, illustrating that generic semantic correspondence is still a particularly challenging task.



















D Additional SPair-U Details

We annotated images using the VGG Image Annotator [11]. We further post-processed the annotations into JSON files replicating the structure of SPair-71k annotations, i.e., per-image annotations and a list of testing pairs. This allows SPair-U to function as a drop-in replacement for SPair-71k evaluation in any semantic correspondence evaluation script. Note that it is designed to be a benchmark of unseen semantic points intended for evaluating the generalization ability of SC models, therefore does not come with a training or validation split. We present the full list of keypoint semantics of SPair-U in Table A3, per-category statistics in Table A4, and some keypoint visualization in Fig. A2.

Table A3: List of SPair-U keypoint semantics.

Aeroplane	front-left, front-right, rear-left, rear-right doors
Bicycle	top and bottom of head tube; front brake; rear brake
Bird	center of back, chest; left wing wrist; right wing wrist
Boat	midpoint of the bow; front-left, front-right, rear-left, rear-right side midpoints
Bottle	center and corner points of label
Bus	top-left, top-right, bottom-left, bottom-right corners of windshield
Car	front-left, front-right, rear-left, rear-right top of the wheel arches
Cat	front-left, front-right, rear-left, rear-right hocks
Chair	leg midpoints; seat edge midpoints; seat center
Cow	left and right shoulder joints; left and right hip joints; left and right centers of the body; middle of back
Dog	front-left, front-right, rear-left, rear-right hocks
Horse	left and right shoulder joints; left and right hip joints
Motorbike	front fender midpoint; seat front edge, seat rear edge; engine compartment center
Person	forehead center; navel; neck base; left hip joint, right hip joint
Plant Pot	center of pot; midpoints of edges; midpoints of rim
Sheep	left and right shoulder joints; left and right hip joints
Train	locomotive rear top-left, top-right, bottom-left, bottom-right corners
Tv	center point; top-left, top-right, bottom-left, bottom-right quadrant centers

Table A4: Per-category statistics for our SPair-U benchmark.

																			Avg
Image count	27	26	27	27	30	27	25	25	26	25	25	27	26	30	27	28	27	27	27
Number of pairs	254	576	480	666	338	304	300	510	552	466	488	420	536	488	744	218	314	600	458
Count of new semantic labels	4	4	4	5	5	4	4	4	9	7	4	4	4	5	5	4	4	5	4.7
Total labeled points	39	74	37	74	71	66	44	64	138	81	72	60	67	62	118	39	50	116	70.7
Average number of visible points	1.4	2.9	1.4	2.7	2.4	2.4	1.8	2.6	5.3	3.1	2.9	2.4	2.5	2.4	3.9	1.4	1.8	4.3	2.6
Number of zero-kp images	3	1	2	0	11	9	0	1	1	2	2	3	2	0	2	10	2	2	2.9
Min keypoint occurrence	8	14	2	11	13	17	10	14	11	8	17	15	16	9	22	9	12	23	12.8
Avg keypoint occurrence	10.8	19.5	10.3	15.8	15.2	17.5	12.0	17.0	16.3	12.6	19.0	16.0	17.8	13.4	24.6	10.8	13.5	24.2	15.9
Max keypoint occurrence	13	25	20	23	19	18	14	21	21	19	20	17	20	21	27	13	15	25	19.5
Avg kp per pair	1.4	2.4	1.2	1.7	2.9	3.4	1.5	1.9	3.8	2.0	2.5	2.0	2.0	1.7	3.6	1.6	1.9	4.3	2.3

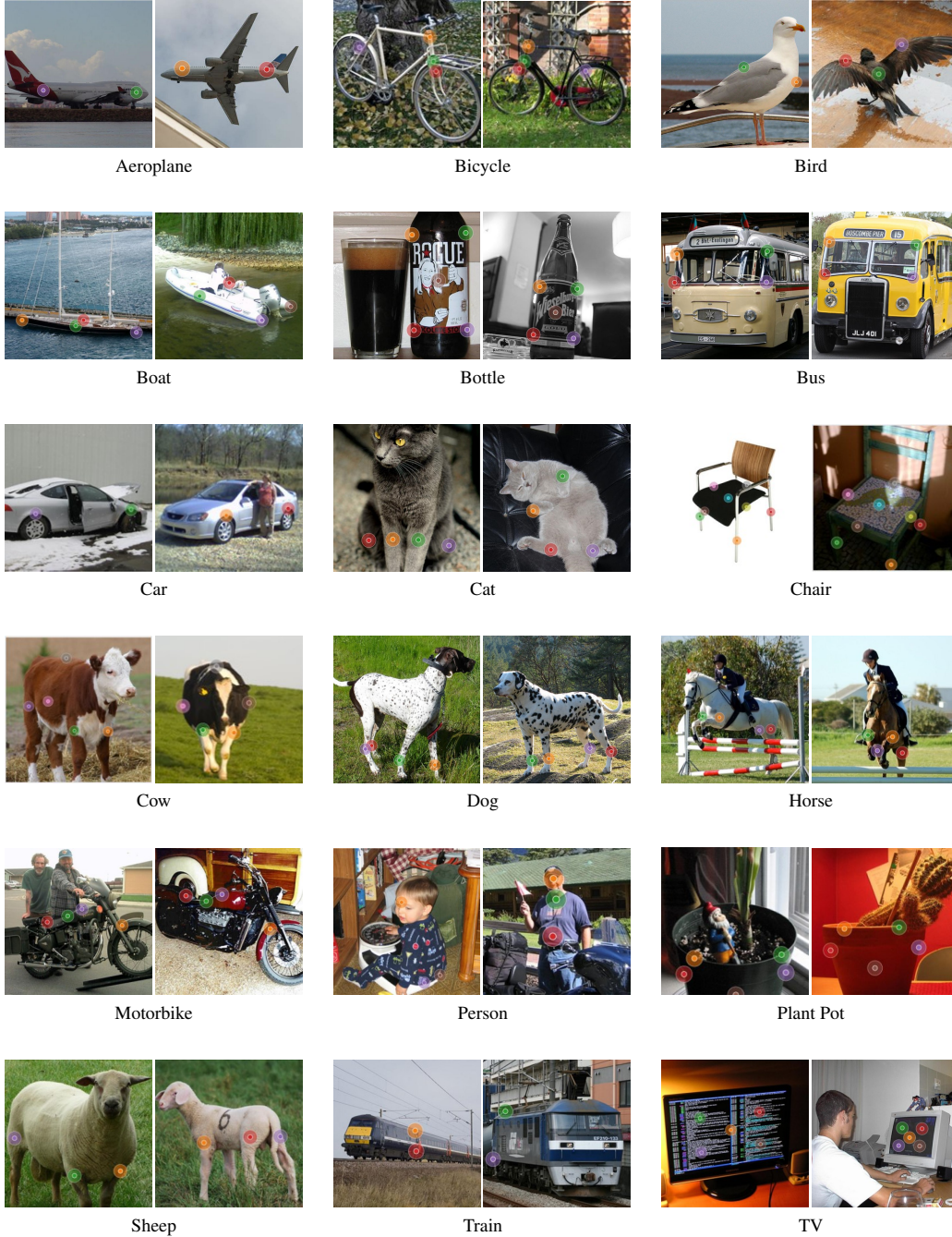


Figure A2: **Visualization of keypoint annotations from SPair-U.** Colors represent keypoint IDs.

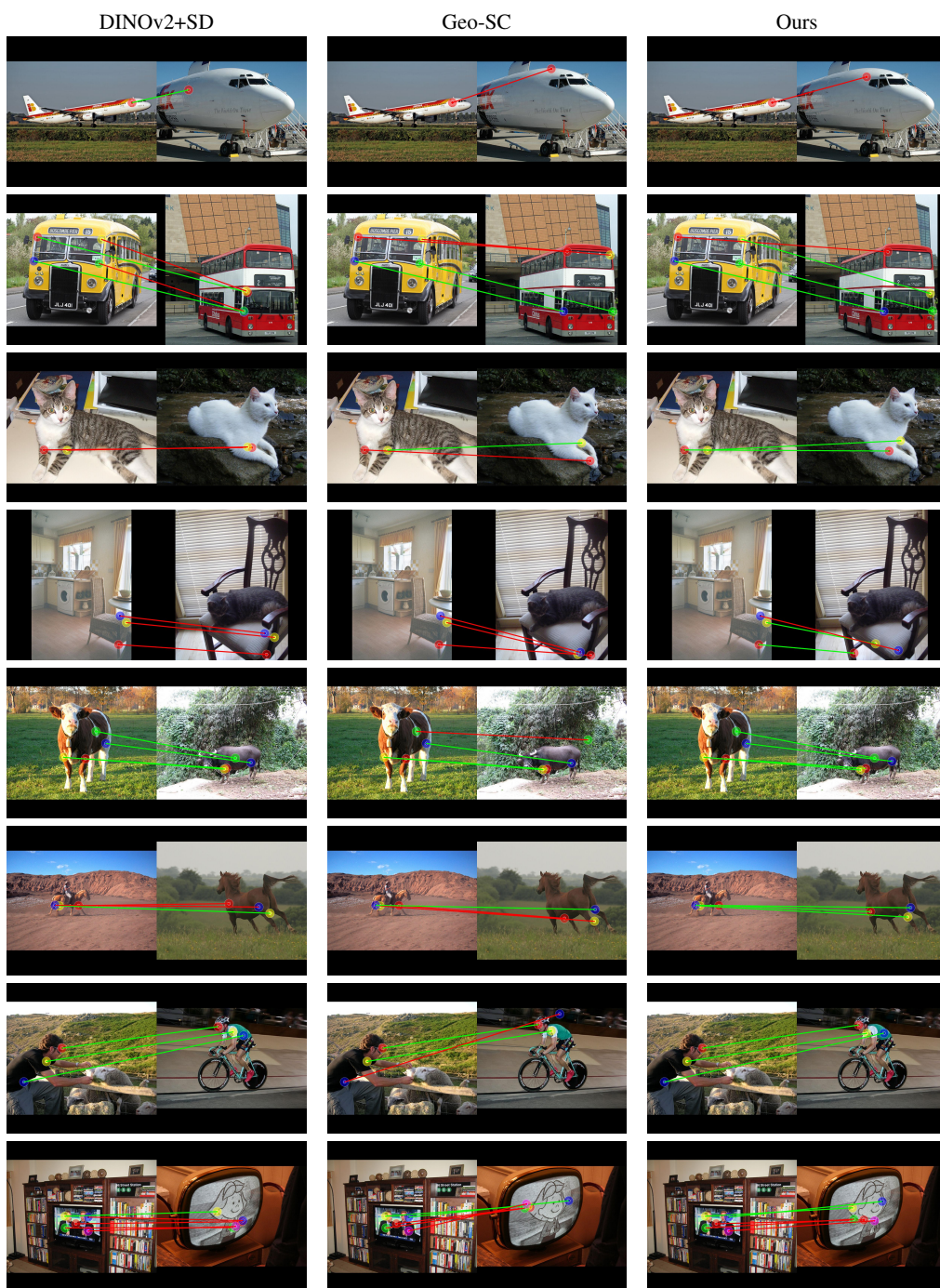


Figure A3: **Visualization matches for SPair-U.** Green lines are correct, red ones are incorrect.